Ultrasonics 125 (2022) 106780

Contents lists available at ScienceDirect

Ultrasonics

journal homepage: www.elsevier.com/locate/ultras

Ultrasonic testing of thick and thin Inconel 625 alloys manufactured by laser powder bed fusion

A. Allam [a,*], O. Alfahmi [a], H. Patel [a], C. Sugino [a], M. Harding [b], M. Ruzzene [c], A. Erturk [a]

[a] G.W. Woodruff School of Mechanical Engineering, Georgia Institute of Technology, Atlanta, 30332, GA, USA
[b] Tronosjet Manufacturing, Charlottetown, C1C 1N2, PE, Canada
[c] Department of Mechanical Engineering, University of Colorado Boulder, Boulder, 80309, CO, USA

ARTICLE INFO

Keywords:
Additive manufacturing
Non-destructive testing
Ultrasonic phased arrays
Laser Doppler vibrometry
Guided waves

ABSTRACT

Additive manufacturing of alloys enables low-volume production of functional metallic components with complex geometries. Ultrasonic testing can ensure the quality of these components and detect typical defects generated during laser powder bed fusion (LPBF). However, it is difficult to find a single ultrasonic inspection technique that can detect defects in the large variety of geometries generated using LPBF. In this work, phased array ultrasonic testing (PAUT) is suggested to inspect thick LPBF components, while guided waves are explored for thin curved ones. PAUT is used to detect cylindrical lack of fusion defects in thick LPBF rectangular parts. Practical defects are generated by reducing the laser power at prespecified locations in the samples. The defects' shape and density are verified using optical microscopy and X-ray computed tomography. Partially fused defects down to 0.25 mm in diameter are experimentally detected using a 10 MHz PAUT probe with the total focusing method post-processing. The experimental results are compared to defect images predicted by finite element simulations. For thin components with curved geometry, guided waves are used to detect powder-filled cylindrical defects. The waves are generated using piezoelectric transducers, and the spatiotemporal wavefield is measured using a scanning laser Doppler vibrometer. Using root-mean-square imaging of the wavefield, defects down to 1 mm are clearly detected despite the complex internal features in the samples.

1. Introduction

Additive manufacturing (AM) enables the production of parts with complex geometry in a cost and energy-effective manner [1]. The flexibility offered by AM is attracting attention from both industry and academia, advancing its use from rapid prototyping to larger-scale manufacturing. Several additive manufacturing processes have been developed and applied in biomedical, aerospace, and automotive fields [2,3]. One of the most prevalent processes for AM of metals is laser powder bed fusion (LPBF) [4–6], in which a piece is formed by locally melting powder layers via a laser beam. Several factors affect the local melting process in LPBF, including beam velocity, shape, and power [5,7,8]. An incompatible parameter, such as insufficient beam power, can lead to defect creation in the manufactured component [9]. These defects might form internally in the part (e.g., internal porosities caused by entrapped gases or lack of fusion) making them difficult to detect and compromising the structural integrity [10–12].

Several non-destructive testing (NDT) techniques have been leveraged for inspecting AM parts, ranging from conventional NDT, such as visual testing (VT), radiographic testing (RT), and ultrasonic testing (UT) to advanced NDT techniques, including X-ray computed tomography (XCT), phased array ultrasonic testing (PAUT), and laser ultrasonics (LU) [13]. In general, XCT is the foremost technique used to inspect additive manufactured parts due to its ability to image part internals accurately with high resolution. However, X-rays are heavily attenuated in dense alloys, such as Inconel 625, which leads to low-quality scans for large samples [14]. On the other hand, UT offers a lower resolution alternative suited for the quality control of AM parts at a low cost with higher accessibility.

Recent work has investigated adapting UT techniques to detect defects in AM parts [13]. The inspection technique varied depending on the AM technology and the size and complexity of the AM part. Wire-arc AM (WAAM) is commonly used to generate large-scale components (typical layer height 1–2 mm compared to tens of μm in LPBF) with typical defects on the order of a few millimeters [15]. This scale is close to what is commonly encountered in the UT inspection of welds, and thus UT [16], LU [17], and PAUT [18,19] techniques have shown promising results in the inspection of WAAM parts. On the other hand, LPBF parts tend to be smaller with finer details and typical defects

* Corresponding author.
E-mail address: a.allam@gatech.edu (A. Allam).

https://doi.org/10.1016/j.ultras.2022.106780
Received 2 January 2022; Received in revised form 30 May 2022; Accepted 31 May 2022
Available online 6 June 2022

on the order of hundreds of microns [11], which is challenging for conventional UT.

Conventional UT has been suggested for the online [20–22] and offline [14,23–26] monitoring of LPBF properties during and after manufacturing. Online monitoring is suitable for verifying the bond quality as the layers are deposited, while an offline approach is more appropriate for further defect detection and material characterization. Kim et al. [25] suggested using offline ultrasonic phase velocity measurements to predict the presence of porosity in 316L stainless steel components. Song et al. [23] used a 15 MHz focused immersion transducer on a positioning system to scan a thick rectangular sample with intentional defects. Individual defects down to 153 μm were detected using this approach. Allam et al. [14] suggested using PAUT for detecting clusters of defects (porosity) in LPBF parts. A defect region generated by reducing the laser power in a cylindrical sample was detected using a 40 element 5 MHz phased array. Honarvar et al. [24] used PAUT in an immersion water tank to detect deliberate defects filled with entrapped unmelted powder in a rectangular sample. A 256-element 50 MHz PAUT probe was used to generate 3D defect images capable of detecting the edges of defects down to 0.75 mm. Marmonier et al. [26] used a 2D PAUT probe to generate 3D images for 0.8 mm spherical defects in LPBF stainless steel parts.

Laser ultrasonics has also been investigated for the inspection of LPBF components [27–30]. In LU, a laser excites or detects ultrasonic waves in the part, making it suitable for complex geometries since it is completely contactless. A laser-induced phased array (LIPA) can image the internal features of the sample using PAUT imaging algorithms such as B-scan or C-scan [31,32], synthetic aperture focusing techniques [33], or the total focusing method (TFM) [34,35]. Cylindrical defects down to 0.5 mm in diameter were imaged in a rectangular sample using LIPA [34].

The UT and LU efforts mentioned so far tested samples at least 5 mm thick. These dimensions are suitable for bulk ultrasonic wave propagation and phased array imaging; however, practical AM parts might have thinner dimensions where many propagation modes exist in the form of guided waves (Lamb waves). Ultrasonic guided waves have been exploited to detect various defect types in thin structures [36]. They have been reliably used to detect delamination and internal cracks in composite materials [37–41], mainly for structural health monitoring applications [42]. However, their use in the inspection of AM components has been limited so far [43].

Lamb waves are dispersive by nature, and many modes with different propagation velocities might exist at the same frequency. Special attention must be given to excite the fewest modes possible in the structure [44–46] and filter the received signal to isolate a specific mode [47–49]. Piezoelectric transducers are commonly employed to excite guided waves [42,50,51]. More specifically, piezoelectric patches are bonded to the surface of the inspected component to provide excellent mechanical coupling. Scanning laser Doppler vibrometry (SLDV) can be used to perform contactless measurements of Lamb waves. SLDV enables spatiotemporal measurement of waves propagating through the scanned thin part, which provides information about its internal structure, such as defects [52–55].

In the present work, we explore using ultrasonic techniques for detecting typical lack of fusion defects generated in LPBF parts due to improper laser beam power. Two techniques are investigated to cover a large subset of the various geometries that can be generated using LPBF. PAUT is based on bulk ultrasonic waves and is well suited for the inspection of thick parts. Using the TFM, PAUT data is converted to 2D images for detecting defects intentionally generated inside a thick LPBF part. The defects are generated by varying the laser power at specific locations inside the sample to cause lack of fusion. The nature of the lack of fusion defects is investigated using optical microscopy and XCT. The experimental measurements are compared to 2D finite element method (FEM) simulations to identify the minimum detectable defect size. PAUT is not well suited for thin shell structures due to the presence of the dead zone, and interface distortions of the image. For thin structures, we investigate using Lamb waves excited using a piezoelectric transducer and captured using an SLDV. Root mean square (RMS) averaging of the frequency–wavenumber filtered data generates images of the defects inside the LPBF parts. The minimum detectable defect size is characterized for both techniques, highlighting the limitations that might prevent its detection.

Table 1
The laser power and power density used at the defect regions of the thick samples. The power density was calculated from the formula in Ref. [14].

Sample #	Laser power (core region) [W]	Energy density [J/mm^3]
1	50	18.5
2	100	37.0
3	200[a]	74
4	300	111

[a]Recommended power by the LPBF system manufacturer.

2. Testing of thick LPBF components

The ability of ultrasonic waves to detect defects in thick LPBF components was tested by printing four 50 mm × 25 mm × 15 mm rectangular samples with internal pin-shaped intentional defect regions (i.e., seeded defects) of varying sizes, as shown in the schematic in Fig. 1a. A Renishaw RenAM 500Q system was used to fabricate the samples. The laser power was varied from the normal value of 200 W to cause a heightened concentration of pore formation in the "pin" regions. The laser power used in the defect regions of each sample is summarized in Table 1, while the standard power of 200 W was used throughout the remainder of the rectangular samples. All other key process parameters were maintained at normal settings.

2.1. Optical microscopy and XCT scanning results

To verify the presence of a higher concentration of print defects in the pin regions, a set of specimens was imaged using optical microscopy and XCT. XCT images were obtained for Samples 1, 2, and 4 through the commercial services of Yxlon Inc. The images were generated using a Yxlon FF85 CT scanner with a (283 kV, 0.35 mA) X-ray beam, five integration frames, and a resolution (voxel size) of 46.3 μm. Two internal cross-sections at the center of Samples 1 and 2 are shown in Fig. 1b and c, respectively. The XCT images of Sample 1 (50 W) show the defects down to 0.25 mm, with the 0.25 mm defect being faintly visible. For Sample 2 (100 W), the 2 mm and 1 mm defects were faintly visible while smaller defects were not detected. The results for Sample 4 (300 W) did not show any visible defects.

To obtain microscope images, the samples were sectioned, exposing the pin region, and polished. Standard polishing down to 0.1 μm colloidal silica was completed, followed by etching using Alders reagent and imaging at 100x magnification. Images for 50 W and 100 W laser power (Samples 1 and 2, respectively) are shown in Figs. 2 and 3, while Samples 3 and 4 (laser power settings of 200 W and 300 W) showed defect concentrations in-line with the bulk material, and hence are not shown. While a high concentration of defects attributed to lack-of-fusion was observed in Samples 1 and 2 at the 2 mm, 1 mm, 0.5 mm, and 0.25 mm pin locations, the 0.125 mm pin region could not be definitively located in any sample, which is expected given the small size.

All the defects detected by optical microscopy appeared in the XCT images except for the 0.5 mm and 0.25 mm defects in Sample 2 (Fig. 3c and d). These defect regions showed a sparse defect density with sub 100 μm pores which presented a challenge for XCT given the large size of the samples, and the significant X-ray attenuation present in dense Inconel alloys.

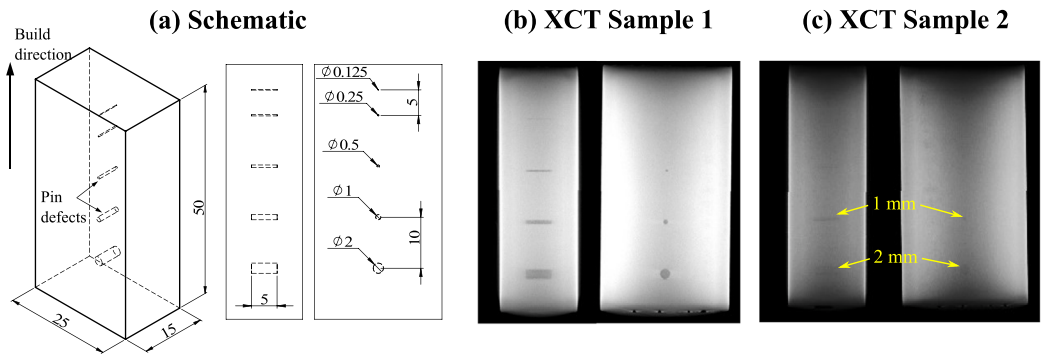

Fig. 1. (a) Schematic of the thick sample showing the intentional pin defect area where the laser power was varied. (b) Sections in the XCT 3D image showing the defects generated in Sample 1 and (c) Sample 2. The 2 mm and 1 mm defects highlighted in Sample 2 were faintly visible.

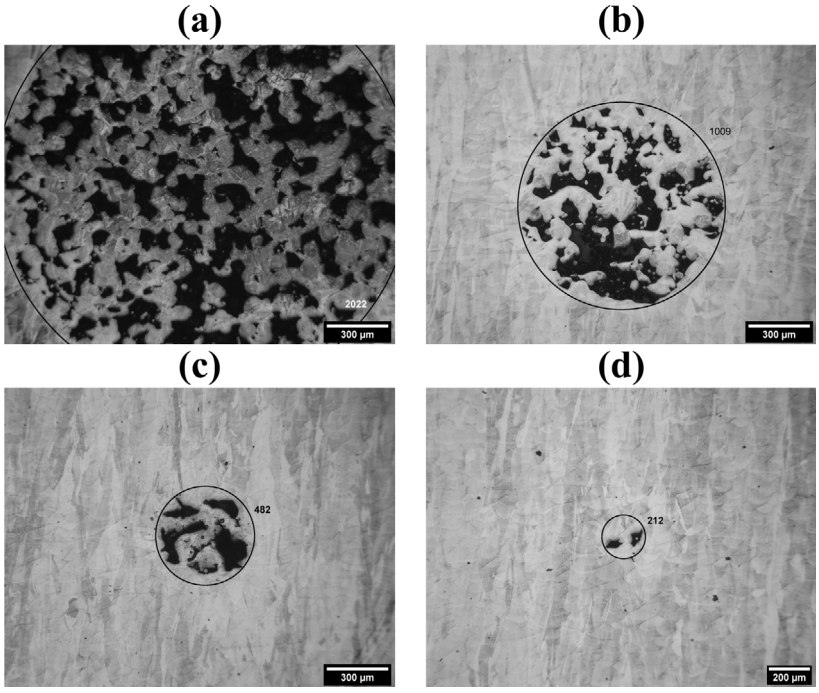

Fig. 2. Optical microscope images of Sample 1 (50 W) showing cross-sections in the (a) 2 mm, (b) 1 mm, (c) 0.5 mm, and (d) 0.25 mm defect regions.

2.2. PAUT imaging

With the microscope and XCT images as a baseline, next a 64-element 10 MHz linear PAUT probe is developed to image the defects in the thick samples. The probe was composed of elements of width 0.2 mm with 0.25 mm pitch and a total length (aperture) of 16 mm. The frequency of the probe was selected to offer a balance between high imaging resolution and low attenuation. The longitudinal wave speed in Inconel 625 (c_l) was measured using pulse-echo to be 5711 m/s, yielding a wavelength of $\lambda = 0.57$ mm at 10 MHz. The 10 MHz probe can resolve defects down to its diffraction limit L_R given by Rayleigh criterion [56]:

$$L_R = 0.61 \frac{\lambda}{\sin\theta} \tag{1}$$

where $\sin\theta$ is the numerical aperture of the array, $\theta = \arctan(D/2z)$, D is the aperture of the probe (16 mm), and z is the depth of the defect. For defects 12.5 mm deep, the resolution of the probe is limited to $L_R = 0.645$ mm. Defects separated by distances smaller than 0.645 mm is expected to appear as a single object in the image.

The PAUT was first simulated numerically using a 2D FEM constructed using COMSOL Multiphysics® [57]. An elastic domain was used to model the samples. The domain was meshed using at least five elements per wavelength at the highest simulated frequency. The optical microscopy images (shown in Figs. 2 and 3) were used to construct the defect geometry in the FEM model. The defects were modeled as free internal boundary conditions in the elastic domain to simulate the air inclusions (pores). The PAUT probe was modeled as an external boundary load to the elastic domain. A time-domain analysis was used to simulate the propagation of elastic longitudinal waves in the samples and their reflection from the defects. A total of 64 simulations were performed to capture the full matrix (R_{ij}) of the array. In each simulation, one element of the PAUT probe was excited, and the response (displacement) of all elements was recorded. The rows of the full matrix (i) represent the excited element, and the columns (j) represent the receiving element. The full matrix was then used to generate the simulated TFM image of the PAUT probe. The TFM image $I(x,z)$ was generated using the relation [58]:

$$I(x,z) = \left| \sum_{i=1}^{N} \sum_{j=1}^{N} R_{ij} \left(\frac{\sqrt{(x_i - x)^2 + z^2}}{c_l} + \frac{\sqrt{(x_j - x)^2 + z^2}}{c_l} \right) \right| \tag{2}$$

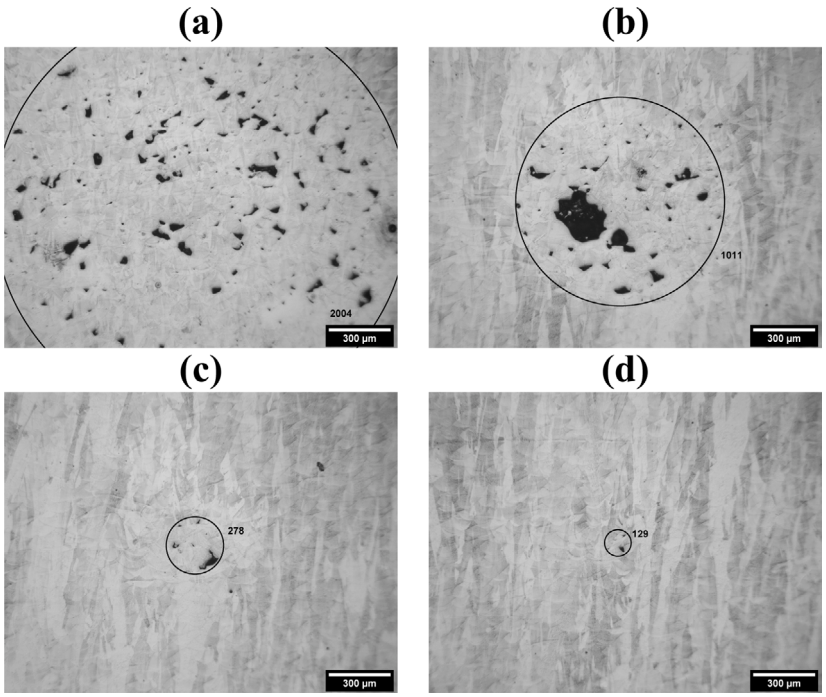

Fig. 3. Optical microscope images of Sample 2 (100 W) showing cross-sections in the (a) 2 mm, (b) 1 mm, (c) 0.5 mm, and (d) 0.25 mm defect regions.

where x and z are the spatial coordinates parallel to the surface of the probe and perpendicular to it, respectively, $\tilde{R}_{ij}(t)$ is the in-phase/quadrature (Hilbert transform) of the full matrix, x_i, x_j are the locations of the transmitting and receiving elements, and $c_l = 5711$ m/s is the longitudinal wave speed in Inconel 625.

Fig. 4 shows the simulated TFM image for Sample 1 and Sample 2 when the PAUT probe was placed at two different locations along the side of the samples, as shown in the inset of each figure. The dead zone near the surface of the probe was not calculated to simplify the figures and highlight the defects. All the defects were visible in the TFM images of Sample 1 (Fig. 4a and b), with the 0.125 mm being faintly visible. For Sample 2, the spacing between the defects extracted from the optical microscopy results was larger than 0.125 mm, so the 0.125 mm defect was not modeled. The defects larger than 0.25 mm were clearly visible in the TFM images for Sample 2 (Fig. 4c and d). The 0.25 mm defect was very faintly visible, as shown in Fig. 4c.

The accuracy of the FEM model is evaluated by comparing its predictions to experimental images obtained using a Verasonics Vantage-64 phased array system with a 64-element PAUT probe supplied by Imasonics. The probe had a center frequency of 10 MHz, a bandwidth of 60%, an element width of 0.2 mm, a pitch of 0.25 mm, a total length of 16 mm, and an elevation of 6 mm. One side of the samples was machined on a milling machine to reduce its surface roughness, and was used as the scanning surface, as shown in Fig. 5. An ultrasonic gel (Olympus D12) was used to ensure good ultrasonic coupling between the PAUT probe and the samples.

Fig. 5a and b show the experimental TFM images for Sample 1 when the probe was placed at two different locations, as shown in the insets. The 0.5 mm and larger defects were clearly detected in the images, while the 0.25 mm defect was barely visible. The noise generated due to the scattering of the ultrasonic waves from the internal structure of the sample prevented the detection of the 0.125 mm defect. The experimental TFM image for Sample 2 is shown in Fig. 5c. Only the 2 mm defect was clearly visible in the images, and the smaller defects were not detected.

By comparing the TFM images obtained using the FEM (Fig. 4) to the experimental images (Fig. 5), it is clear that the 2D FEM models overpredict the reflections from the defects. The 2D simplified FEM models assume that the defects are elongated in the out-of-plane direction; however, in reality, the defects are spheroidal in nature. Moreover, the FEM model does not account for the noise generated from the microstructure of the AM samples, which hindered detecting smaller and lower density defects. The deviation was more significant for the low defect density Sample 2. Only the 2 mm defect was detected experimentally, whereas the defects down to 0.5 mm were clearly visible in the FEM results. The smaller defects might be experimentally detected by employing signal denoising [59] or super-resolution imaging techniques [56,60].

3. Testing of thin LPBF components

For the ultrasonic inspection of thin parts, conventional PAUT techniques fail due to the proximity of defects to the part surface and repeated reflections from each surface. By contrast, Lamb waves propagating within the plane of the thin part can travel over long distances without reflections while maintaining sensitivity to defects within the part thickness [61]. Unlike bulk longitudinal or shear waves in metals, there are multiple Lamb wave modes excitable at any given frequency, and each Lamb wave mode is highly dispersive. For an isotropic medium with longitudinal wave speed c_l, shear wave speed c_s, and thickness d, Lamb wave modes satisfy

$$\frac{\tanh(\beta d/2)}{\tanh(\alpha d/2)} = \frac{4\alpha\beta k^2}{(k^2+\beta^2)^2} \tag{3}$$

for symmetric modes, and

$$\frac{\tanh(\beta d/2)}{\tanh(\alpha d/2)} = \frac{(k^2+\beta^2)^2}{4\alpha\beta k^2} \tag{4}$$

for asymmetric modes, where

$$\alpha^2 = k^2 - \frac{\omega^2}{c_l^2}, \quad \beta^2 = k^2 - \frac{\omega^2}{c_s^2} \tag{5}$$

where ω and k are the frequency and wavenumber of the wave, respectively. Symmetric and asymmetric Lamb waves exhibit through-thickness deformation that is symmetric or asymmetric about the mid-plane of the waveguide, respectively.

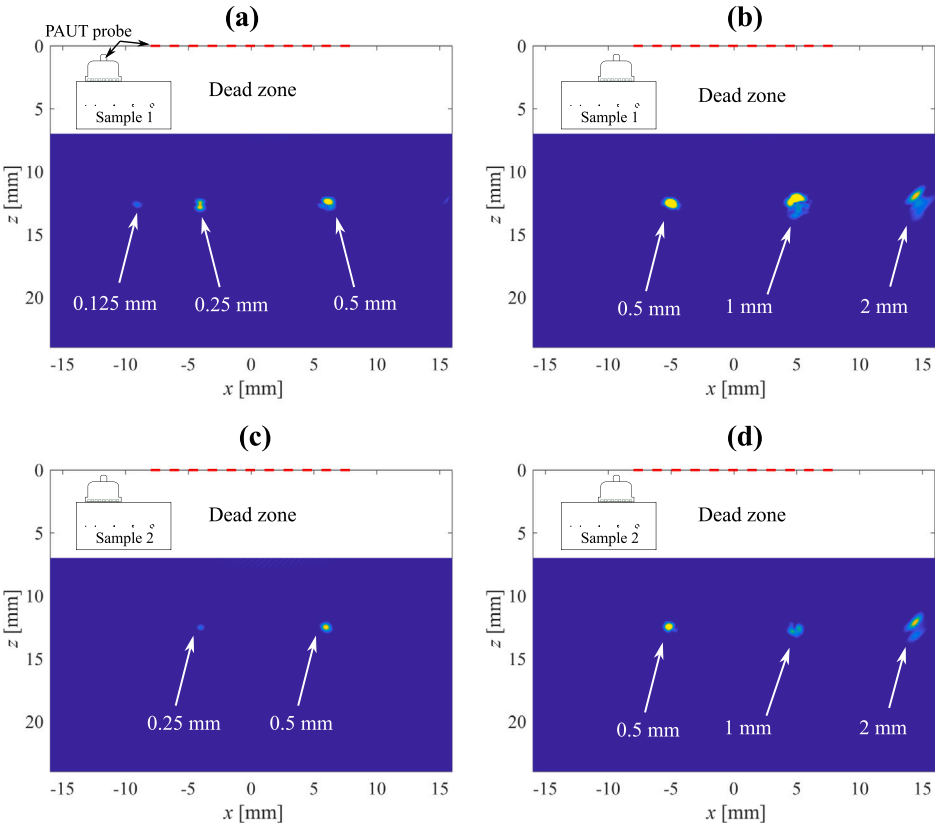

Fig. 4. TFM image generated using the FEM for the defect density extracted from (a&b) Sample 1 and (c&d) Sample 2. The location of the PAUT probe with respect to the sample is shown in the insets.

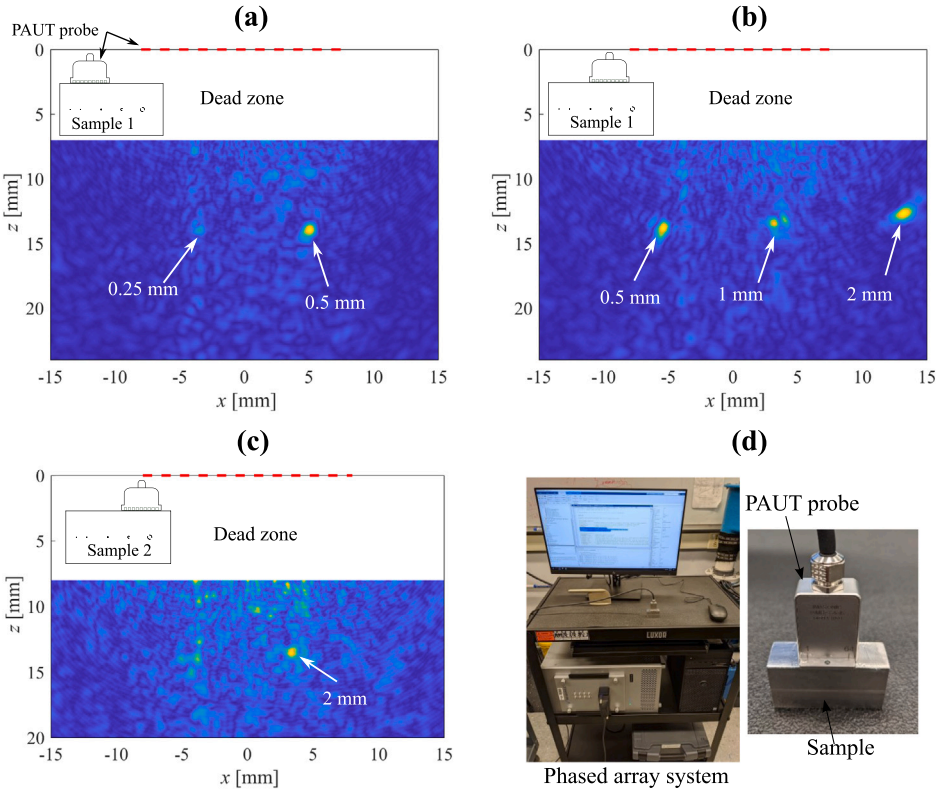

Fig. 5. (a) Experimental TFM image showing the 0.25 mm and the 0.5 mm defects in Sample 1. (b) TFM image for Sample 1 when the array is moved to image the 1 mm and 2 mm defects. (c) TFM image for Sample 2 showing the 2 mm defect. (d) Experimental setup used for imaging the defects using a PAUT system.

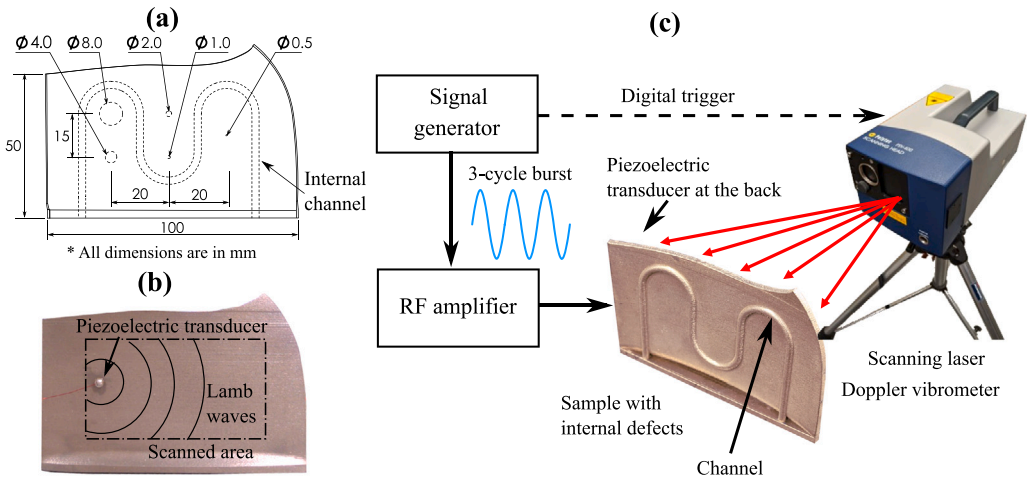

Fig. 6. (a) The geometry of the thin samples showing the location and size of the defect regions and the internal channel. (b) The front side of the thin sample showing the 3 mm diameter piezoelectric disk used for exciting Lamb waves in the sample. (c) SLDV setup for imaging the thin samples showing the backside of the functional thin sample with the channel.

We consider two relatively thin (2 mm thick) curved LPBF components with identical external geometry, a functional part with an internal channel and a simplified one without the channel. Both parts have five intentionally introduced internal defects of thickness 1 mm, and diameter 8 mm, 4 mm, 2 mm, 1 mm, and 0.5 mm to characterize which feature sizes are detectable using Lamb waves. The defects were generated by disabling the LPBF laser at the defect location, and as a result, they are filled with unfused powder during manufacturing. The geometry of the thin samples is shown in Fig. 6a, and the front side of the fabricated samples is shown in Fig. 6b, with the back side shown in Fig. 6c for the functional sample.

Scanning laser Doppler vibrometry is a contactless measurement technique that uses a laser beam to measure surface velocity v via the Doppler effect at multiple scan points (x, y). The full wavefield $v(x, y, t)$ can be measured experimentally by synchronizing repeated measurements at each point. This data is then processed using the 3D fast Fourier transform (FFT) [62] to obtain its spectral representation, $V(k_x, k_y, \omega)$, where k_x and k_y are the x- and y-components of the two-dimensional wavevector $\boldsymbol{k}$. Energy localization in the spectrum $|V(k_x, k_y, \omega)|$ denotes the experimentally measured Lamb waves, which are then compared to numerically predicted dispersion curves to identify each measured wave mode. For simplicity, it is assumed that the part is isotropic, flat, and has a uniform thickness, and only propagation in the x-direction of the scan is considered.

3.1. Lamb wave characterization

The Lamb wave dispersion curves of the components are evaluated experimentally using the setup shown in Fig. 6c. Lamb waves were excited using a 3 mm diameter by 0.4 mm thick piezoelectric disk (SMD03T04S311 supplied by STEMiNC) bonded to the surface of the part using an epoxy adhesive and excited with a 3-cycle tone burst centered at 850 kHz. The surface velocity of the sample was measured using a Polytec PSV-500 SLDV, and the corresponding spectrum $|V(k_x, \omega)|$ is shown in Fig. 7, together with the numerically predicted dispersion curves and labeled Lamb wave modes. Several Lamb wave modes are excited by the piezoelectric transducer, including the fundamental modes A0 and S0, and the higher-order A1 and S1 modes. A good agreement between the experimental and numerical results is observed for all the detected modes, with some noticable mismatch in the S0 mode. The discrepancy in this symmetric mode is likely caused by the anisotropy generated during LPBF printing, and there might be potential contribution from the out-of-plane geometric features of the sample as well.

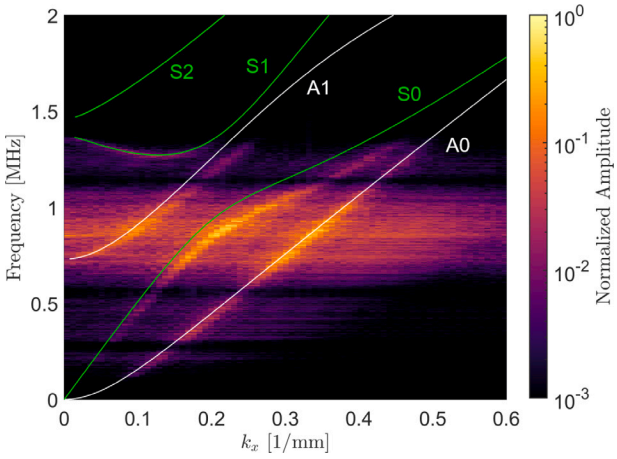

Fig. 7. Experimental (heatmap) and numerical (solid lines) frequency–wavenumber dispersion results.

3.2. Lamb wave-based detection of defects

Similar to the measurement of Lamb wave dispersion curves, internal features can be imaged using the full wavefield obtained through SLDV measurements [63,64]. Wave reflection and mode conversion near defects result in a local increase in the RMS surface velocity, allowing the SLDV to image defects across the entire scanned area, given a sufficient incident wave energy. The thin LPBF parts with and without an internal channel were excited using a piezo disk (as in Section 3.1), and the velocity field was measured using a spatial resolution of 0.5 mm and a sample rate of 12.5 MHz. The measured time signal for each point was averaged 500 times to minimize the noise level. A total of 12 835 points were scanned with 3 ms per measurement and a total of 5.5 h to perform the complete scan. The number of averages and resolution was chosen conservatively to maximize the image quality and detect the minimum defect size. Faster scans with a resolution of 1 mm and 100 averages can be performed in 3.2 min with acceptable image quality. The resulting images (i.e., RMS velocity fields) are shown in Fig. 8.

All defects except the 0.5 mm one were clearly visible for both the simplified and the functional sample with the channel. The internal channel was clearly detected, and it did not affect the detection of the

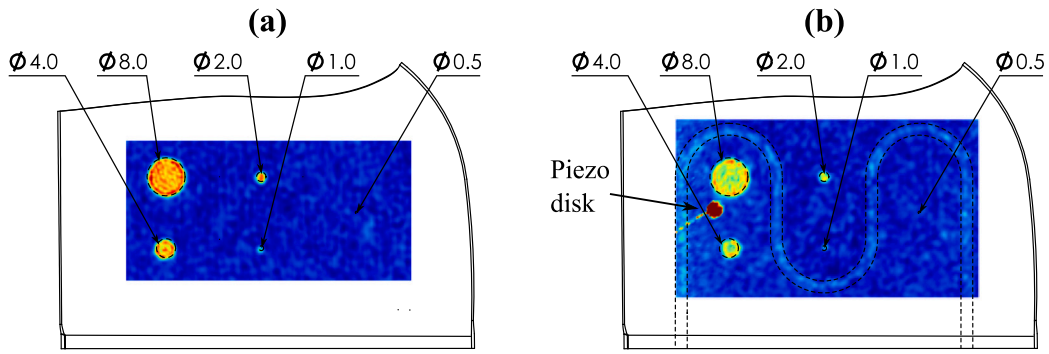

Fig. 8. (a) Experimental SLDV RMS image of the part without an internal channel. (b) Experimental SLDV RMS image of the part with an internal channel. All defects except the 0.5 mm defect are accurately imaged in both cases. The internal channel in (b) is most clearly imaged near the excitation source.

smaller defects away from the piezoelectric disk used for the excitation. The simplified sample (without the channel) was sanded down using a 200 grit sandpaper to reduce its surface roughness, while the functional sample was scanned as manufactured. The smooth surface helped reduce the measurement noise of the simplified sample (Fig. 8a) compared to the rough surface (Fig. 8b). Nevertheless, the internal defects were clearly detectable without additional post-processing of the samples.

4. Conclusions and future work

Ultrasonic testing (UT) was investigated as a quality assurance tool for AM parts manufactured using laser powder bed fusion (LPBF). UT was successfully implemented to detect clusters of defects generated during LPBF. However, successful detection is contingent on selecting a suitable UT technology for the part geometry.

Phased array UT (PAUT) was suitable for detecting deep defects in thick components. PAUT was used to inspect thick rectangular samples with partially fused cylindrical defects. The nature of the defects was studied using X-ray CT scanning and optical microscopy. Defects down to 0.25 mm were detected when the laser power in the defect area was 25% of the recommended level. When the laser power was set to 50%, lower defect densities were generated, and only 2 mm defects were detected experimentally. Comparing experimental defect images to images generated by the finite element method revealed that scattering from grain boundaries (AM microstructure) obscured smaller defects and prohibited their detection using the total focusing method imaging.

While PAUT is suitable for the inspection of thick parts with flat surfaces, it is challenging to use with thin parts with curved surfaces. Multiple reflections from the surfaces compounded with mode conversion and non uniform diffraction and reflection from the sample surface distorts the phased array image. Current state-of-the-art PAUT imaging techniques do not effectively address these issues. On the other hand, guided waves were well suited for thin curved parts. They propagate in parts with complex curvature and internal features. Piezoelectric transducers were used to excite thin-walled functional samples with intentional powder-filled defects, and the generated wavefield was measured using a scanning laser Doppler vibrometer. Cylindrical defects with a diameter down to 1 mm were clearly imaged using root mean square wavefield averaging. The defects were detected despite the rough curved surface of the manufactured part and the presence of complex internal features.

Our results show that ultrasonic techniques can be used to inspect thick parts with flat surfaces and thin parts with complex surfaces. More work is needed to develop a unified approach to image LPBF parts with arbitrary geometry. The PAUT approach might be expanded to excite and receive guided waves [65] in thin structures; however, flexible phased arrays or special immersion setups might be required to scan parts with complex surfaces. On the other hand, Laser-induced phased arrays (LIPA) might be used to synthesize phased arrays on complex surfaces enabling scanning laser vibrometry to image thick structures with complex surfaces [35]. In both approaches, more work is needed to tailor imaging algorithms to address the complexity of imaging a part with a complex external surface. These algorithms can be developed with the aid of numerical simulations of arbitrary surfaces; however, capturing the microstructure generated by LPBF printing is important for a realistic prediction of the ultrasonic signal. A detailed model that captures the microstructure and anisotropy is beneficial for accurate sizing of the defects.

Declaration of competing interest

The authors declare that they have no known competing financial interests or personal relationships that could have appeared to influence the work reported in this paper.

References

[1] W.E. Frazier, Metal additive manufacturing: a review, J. Mater. Eng. Perform. 23 (6) (2014) 1917–1928, http://dx.doi.org/10.1007/s11665-014-0958-z.

[2] N. Guo, M.C. Leu, Additive manufacturing: Technology, applications and research needs, Front. Mech. Eng. 8 (3) (2013) 215–243, http://dx.doi.org/10.1007/s11465-013-0248-8.

[3] C. Tan, F. Weng, S. Sui, Y. Chew, G. Bi, Progress and perspectives in laser additive manufacturing of key aeroengine materials, Int. J. Mach. Tools Manuf. 170 (2021) 103804, http://dx.doi.org/10.1016/j.ijmachtools.2021.103804.

[4] D. Herzog, V. Seyda, E. Wycisk, C. Emmelmann, Additive manufacturing of metals, Acta Mater. 117 (2016) 371–392, http://dx.doi.org/10.1016/j.actamat.2016.07.019.

[5] L. Tonelli, A. Fortunato, L. Ceschini, CoCr alloy processed by selective laser melting (SLM): Effect of laser energy density on microstructure, surface morphology, and hardness, J. Manuf. Process. 52 (2020) 106–119, http://dx.doi.org/10.1016/j.jmapro.2020.01.052.

[6] S. Sanchez, P. Smith, Z. Xu, G. Gaspard, C.J. Hyde, W.W. Wits, I.A. Ashcroft, H. Chen, A.T. Clare, Powder bed fusion of nickel-based superalloys: A review, Int. J. Mach. Tools Manuf. 165 (2021) 103729, http://dx.doi.org/10.1016/j.ijmachtools.2021.103729.

[7] A. Bauereiß, T. Scharowsky, C. Körner, Defect generation and propagation mechanism during additive manufacturing by selective beam melting, J. Mater Process. Technol. 214 (11) (2014) 2522–2528, http://dx.doi.org/10.1016/j.jmatprotec.2014.05.002.

[8] L.E. Criales, Y.M. Arısoy, B. Lane, S. Moylan, A. Donmez, T. Özel, Laser powder bed fusion of nickel alloy 625: experimental investigations of effects of process parameters on melt pool size and shape with spatter analysis, Special Issue on the State-of-the-Art in North American Manufacturing Research, Int. J. Mach. Tools Manuf. 121 (2017) 22–36, http://dx.doi.org/10.1016/j.ijmachtools.2017.03.004.

[9] Y. Xiang, S. Zhang, Z. Wei, J. Li, P. Wei, Z. Chen, L. Yang, L. Jiang, Forming and defect analysis for single track scanning in selective laser melting of Ti6Al4V, Appl. Phys. A 124 (10) (2018) 685, http://dx.doi.org/10.1007/s00339-018-2056-9.

[10] B.M. Sharratt, Non-Destructive Techniques and Technologies for Qualification of Additive Manufactured Parts and Processes, Contract Report DRDC-RDDC-2015-C035, Sharratt Research & Consulting Inc., Victoria, BC, Canada, 2015.

[11] E.O. Olakanmi, R.F. Cochrane, K.W. Dalgarno, A review on selective laser sintering/melting (SLS/SLM) of aluminium alloy powders: processing, microstructure, and properties, Prog. Mater. Sci. 74 (2015) 401–477, http://dx.doi.org/10.1016/j.pmatsci.2015.03.002.

[12] S.M.H. Hojjatzadeh, N.D. Parab, Q. Guo, M. Qu, L. Xiong, C. Zhao, L.I. Escano, K. Fezzaa, W. Everhart, T. Sun, L. Chen, Direct observation of pore formation mechanisms during LPBF additive manufacturing process and high energy density laser welding, Int. J. Mach. Tools Manuf. 153 (2020) 103555, http://dx.doi.org/10.1016/j.ijmachtools.2020.103555.

[13] F. Honarvar, A. Varvani-Farahani, A review of ultrasonic testing applications in additive manufacturing: defect evaluation, material characterization, and process control, Ultrasonics 108 (2020) 106227, http://dx.doi.org/10.1016/j.ultras.2020.106227.

[14] A. Allam, C. Sugino, M. Harding, D.P. Bishop, A. Erturk, M. Ruzzene, Phased array ultrasonic testing of inconel 625 produced by selective laser melting, ASME J. Nondestruct. Eval. 4 (041006) (2021) http://dx.doi.org/10.1115/1.4050963.

[15] S.W. Williams, F. Martina, A.C. Addison, J. Ding, G. Pardal, P. Colegrove, Wire + arc additive manufacturing, Mater. Sci. Technol. 32 (7) (2016) 641–647, http://dx.doi.org/10.1179/1743284715Y.0000000073.

[16] A. Lopez, R. Bacelar, I. Pires, T.G. Santos, J.P. Sousa, L. Quintino, Non-destructive testing application of radiography and ultrasound for wire and arc additive manufacturing, Addit. Manuf. 21 (2018) 298–306, http://dx.doi.org/10.1016/j.addma.2018.03.020.

[17] Y. Zeng, X. Wang, X. Qin, L. Hua, M. Xu, Laser ultrasonic inspection of a wire + arc additive manufactured (WAAM) sample with artificial defects, Ultrasonics 110 (2021) 106273, http://dx.doi.org/10.1016/j.ultras.2020.106273.

[18] A.B. Lopez, J. Santos, J.P. Sousa, T.G. Santos, L. Quintino, Phased array ultrasonic inspection of metal additive manufacturing parts, J. Nondestruct. Eval. 38 (3) (2019) 62, http://dx.doi.org/10.1007/s10921-019-0600-y.

[19] A. Chabot, N. Laroche, E. Carcreff, M. Rauch, J.-Y. Hascoët, Towards defect monitoring for metallic additive manufacturing components using phased array ultrasonic testing, J. Intell. Manuf. 31 (5) (2020) 1191–1201, http://dx.doi.org/10.1007/s10845-019-01505-9.

[20] H. Rieder, M. Spies, J. Bamberg, B. Henkel, On- and offline ultrasonic characterization of components built by SLM additive manufacturing, AIP Conf. Proc. 1706 (1) (2016) 130002, http://dx.doi.org/10.1063/1.4940605.

[21] V.K. Nadimpalli, L. Yang, P.B. Nagy, In-situ interfacial quality assessment of ultrasonic additive manufacturing components using ultrasonic NDE, NDT E Int. 93 (2018) 117–130, http://dx.doi.org/10.1016/j.ndteint.2017.10.004.

[22] T. Hayashi, N. Mori, T. Ueno, Non-contact imaging of subsurface defects using a scanning laser source, Ultrasonics 119 (2022) 106560, http://dx.doi.org/10.1016/j.ultras.2021.106560.

[23] Y. Song, X. Zi, Y. Fu, X. Li, C. Chen, K. Zhou, Nondestructive testing of additively manufactured material based on ultrasonic scattering measurement, Measurement 118 (2018) 105–112, http://dx.doi.org/10.1016/j.measurement.2018.01.020.

[24] F. Honarvar, S. Patel, M. Vlasea, H. Amini, A. Varvani-Farahani, Nondestructive characterization of laser powder bed fusion components using high-frequency phased array ultrasonic testing, J. Mater. Eng. Perform. (2021) http://dx.doi.org/10.1007/s11665-021-05988-7.

[25] C. Kim, H. Yin, A. Shmatok, B.C. Prorok, X. Lou, K.H. Matlack, Ultrasonic nondestructive evaluation of laser powder bed fusion 316l stainless steel, Addit. Manuf. 38 (2021) 101800, http://dx.doi.org/10.1016/j.addma.2020.101800.

[26] M. Marmonier, S. Robert, J. Laurent, C. Prada, Real-time 3D imaging with Fourier-domain algorithms and matrix arrays applied to non-destructive testing, Ultrasonics 124 (2022) 106708, http://dx.doi.org/10.1016/j.ultras.2022.106708.

[27] S.P. Santospirito, R. Łopatka, D. Cerniglia, K. Słyk, B. Luo, D. Panggabean, J. Rudlin, Defect detection in laser powder deposition components by laser thermography and laser ultrasonic inspections, in: Frontiers in Ultrafast Optics: Biomedical, Scientific, and Industrial Applications XIII, Vol. 8611, International Society for Optics and Photonics, 2013, p. 86111N, http://dx.doi.org/10.1117/12.2006361.

[28] S. Everton, P. Dickens, C. Tuck, B. Dutton, Using laser ultrasound to detect subsurface defects in metal laser powder bed fusion components, JOM 70 (3) (2018) 378–383, http://dx.doi.org/10.1007/s11837-017-2661-7.

[29] G. Davis, R. Nagarajah, S. Palanisamy, R.A.R. Rashid, P. Rajagopal, K. Balasubramaniam, Laser ultrasonic inspection of additive manufactured components, Int. J. Adv. Manuf. Technol. 102 (5) (2019) 2571–2579, http://dx.doi.org/10.1007/s00170-018-3046-y.

[30] J. Zhang, J. Wu, X. Zhao, S. Yuan, G. Ma, G. Ma, J. Li, T. Dai, H. Chen, B. Yang, H. Ding, Laser ultrasonic imaging for defect detection on metal additive manufacturing components with rough surfaces, Appl. Opt. AO 59 (33) (2020) 10380–10388, http://dx.doi.org/10.1364/AO.405284.

[31] D. Cerniglia, M. Scafidi, A. Pantano, J. Rudlin, Inspection of additive-manufactured layered components, Ultrasonics 62 (2015) 292–298, http://dx.doi.org/10.1016/j.ultras.2015.06.001.

[32] J. Yu, D. Zhang, H. Li, C. Song, X. Zhou, S. Shen, G. Zhang, Y. Yang, H. Wang, Detection of internal holes in additive manufactured ti-6al-4v part using laser ultrasonic testing, Appl. Sci. 10 (1) (2020) 365, http://dx.doi.org/10.3390/app10010365.

[33] D. Lévesque, C. Bescond, M. Lord, X. Cao, P. Wanjara, J.-P. Monchalin, Inspection of additive manufactured parts using laser ultrasonics, AIP Conf. Proc. 1706 (1) (2016) 130003, http://dx.doi.org/10.1063/1.4940606.

[34] T. Stratoudaki, Y. Javadi, W. Kerr, P.D. Wilcox, D. Pieris, M. Clark, Laser induced phased arrays for remote ultrasonic imaging of additive manufactured components, in: 57th Annual Conference of the British Institute of Non-Destructive Testing, NDT 2018, GBR, 2018, pp. 174–182.

[35] D. Pieris, T. Stratoudaki, Y. Javadi, P. Lukacs, S. Catchpole-Smith, P.D. Wilcox, A. Clare, M. Clark, Laser induced phased arrays (LIPA) to detect nested features in additively manufactured components, Mater. Des. 187 (2020) 108412, http://dx.doi.org/10.1016/j.matdes.2019.108412.

[36] V. Giurgiutiu, C. Soutis, Guided wave methods for structural health monitoring, in: Encyclopedia of Aerospace Engineering, American Cancer Society, 2010.

[37] H. Sohn, D. Dutta, J.Y. Yang, H.J. Park, M. DeSimio, S. Olson, E. Swenson, Delamination detection in composites through guided wave field image processing, Compos. Sci. Technol. 71 (9) (2011) 1250–1256, http://dx.doi.org/10.1016/j.compscitech.2011.04.011.

[38] S. Mustapha, L. Ye, D. Wang, Y. Lu, Assessment of debonding in sandwich CF/EP composite beams using A0 lamb wave at low frequency, Compos. Struct. 93 (2) (2011) 483–491, http://dx.doi.org/10.1016/j.compstruct.2010.08.032.

[39] Z. Su, L. Ye, Y. Lu, Guided lamb waves for identification of damage in composite structures: A review, J. Sound Vib. 295 (3) (2006) 753–780, http://dx.doi.org/10.1016/j.jsv.2006.01.020.

[40] S.M.H. Hosseini, S. Duczek, U. Gabbert, Damage localization in plates using mode conversion characteristics of ultrasonic guided waves, J. Nondestruct. Eval. 33 (1) (2014) 152–165, http://dx.doi.org/10.1007/s10921-013-0211-y.

[41] Y.-K. An, Y. Kwon, H. Sohn, Noncontact laser ultrasonic crack detection for plates with additional structural complexities, Struct. Health Monit. 12 (5–6) (2013) 522–538, http://dx.doi.org/10.1177/1475921713500515.

[42] M. Mitra, S. Gopalakrishnan, Guided wave based structural health monitoring: A review, Smart Mater. Struct. 25 (5) (2016) 053001, http://dx.doi.org/10.1088/0964-1726/25/5/053001.

[43] G. Davis, P. Rajagopal, K. Balasubramaniam, S. Palanisamy, R. Nagarajah, Laser generation of narrowband lamb waves for in-situ inspection of additively manufactured metal components, AIP Conf. Proc. 2102 (1) (2019) 070001, http://dx.doi.org/10.1063/1.5099801.

[44] E.F. Crawley, J. de Luis, Use of piezoelectric actuators as elements of intelligent structures, AIAA J. 25 (10) (1987) 1373–1385, http://dx.doi.org/10.2514/3.9792.

[45] P.D. Wilcox, R.P. Dalton, M.J.S. Lowe, P. Cawley, Mode and transducer selection for long range lamb wave inspection, Key Eng. Mater. 167–168 (1999) 152–161, http://dx.doi.org/10.4028/www.scientific.net/KEM.167-168.152.

[46] V. Giurgiutiu, Tuned lamb wave excitation and detection with piezoelectric wafer active sensors for structural health monitoring, J. Intell. Mater. Syst. Struct. 16 (4) (2005) 291–305, http://dx.doi.org/10.1177/1045389X05050106.

[47] M. Ruzzene, Frequency–wavenumber domain filtering for improved damage visualization, Smart Mater. Struct. 16 (6) (2007) 2116–2129, http://dx.doi.org/10.1088/0964-1726/16/6/014.

[48] T.E. Michaels, J.E. Michaels, M. Ruzzene, Frequency–wavenumber domain analysis of guided wavefields, Ultrasonics 51 (4) (2011) 452–466, http://dx.doi.org/10.1016/j.ultras.2010.11.011.

[49] Z. Tian, L. Yu, Lamb wave frequency–wavenumber analysis and decomposition, J. Intell. Mater. Syst. Struct. 25 (9) (2014) 1107–1123, http://dx.doi.org/10.1177/1045389X14521875.

[50] S. Grondel, C. Paget, C. Delebarre, J. Assaad, K. Levin, Design of optimal configuration for generating A0 lamb mode in a composite plate using piezoceramic transducers, J. Acoust. Soc. Am. 112 (1) (2002) 84–90, http://dx.doi.org/10.1121/1.1481062.

[51] H. Mei, M.F. Haider, R. Joseph, A. Migot, V. Giurgiutiu, Recent advances in piezoelectric wafer active sensors for structural health monitoring applications, Sensors 19 (2) (2019) 383, http://dx.doi.org/10.3390/s19020383.

[52] Y.-K. An, B. Park, H. Sohn, Complete noncontact laser ultrasonic imaging for automated crack visualization in a plate, Smart Mater. Struct. 22 (2) (2013) 025022, http://dx.doi.org/10.1088/0964-1726/22/2/025022.

[53] J. Rao, M. Ratassepp, Z. Fan, Guided wave tomography based on full waveform inversion, IEEE Trans. Ultrason. Ferroelectr. Freq. Control 63 (5) (2016) 737–745, http://dx.doi.org/10.1109/TUFFC.2016.2536144.

[54] B.I.S. Murat, P. Khalili, P. Fromme, Scattering of guided waves at delaminations in composite plates, J. Acoust. Soc. Am. 139 (6) (2016) 3044–3052, http://dx.doi.org/10.1121/1.4953016.

[55] P. Aryan, A. Kotousov, C.T. Ng, B.S. Cazzolato, A baseline-free and non-contact method for detection and imaging of structural damage using 3D laser vibrometry, Struct. Control Health Monit. 24 (4) (2017) e1894, http://dx.doi.org/10.1002/stc.1894.

[56] H. Song, Y. Yang, Super-resolution visualization of subwavelength defects via deep learning-enhanced ultrasonic beamforming: A proof-of-principle study, NDT E Int. 116 (2020) 102344, http://dx.doi.org/10.1016/j.ndteint.2020.102344.

[57] Inc COMSOL, COMSOL multiphysics reference manual, version 5.4, 2018.

[58] C. Holmes, B.W. Drinkwater, P.D. Wilcox, Post-processing of the full matrix of ultrasonic transmit–receive array data for non-destructive evaluation, NDT E Int. 38 (8) (2005) 701–711, http://dx.doi.org/10.1016/j.ndteint.2005.04.002.

[59] W. Xu, X. Li, J. Zhang, Z. Xue, J. Cao, Ultrasonic signal enhancement for coarse grain materials by machine learning analysis, Ultrasonics 117 (2021) 106550, http://dx.doi.org/10.1016/j.ultras.2021.106550.

[60] H. Song, Y. Yang, Noncontact super-resolution guided wave array imaging of subwavelength defects using a multiscale deep learning approach, Struct. Health Monit. 20 (4) (2021) 1904–1923, http://dx.doi.org/10.1177/1475921720942958.

[61] D. Alleyne, P. Cawley, The interaction of lamb waves with defects, IEEE Trans. Ultrason. Ferroelectr. Freq. Control 39 (3) (1992) 381–397, http://dx.doi.org/10.1109/58.143172.

[62] D. Alleyne, P. Cawley, A 2-dimensional Fourier transform method for the quantitative measurement of lamb modes, in: IEEE Symposium on Ultrasonics, 1990, pp. 1143–1146 vol.2, http://dx.doi.org/10.1109/ULTSYM.1990.171541.

[63] L. Mallet, B.C. Lee, W.J. Staszewski, F. Scarpa, Structural health monitoring using scanning laser vibrometry: II. lamb waves for damage detection, Smart Mater. Struct. 13 (2) (2004) 261–269, http://dx.doi.org/10.1088/0964-1726/13/2/003.

[64] W.J. Staszewski, B.C. Lee, R. Traynor, Fatigue crack detection in metallic structures with lamb waves and 3D laser vibrometry, Meas. Sci. Technol. 18 (3) (2007) 727–739, http://dx.doi.org/10.1088/0957-0233/18/3/024.

[65] G. Veit, P. Bélanger, An ultrasonic guided wave excitation method at constant phase velocity using ultrasonic phased array probes, Ultrasonics 102 (2020) 106039, http://dx.doi.org/10.1016/j.ultras.2019.106039.